Nanoscale

COMMUNICATION

View Article Online
View Journal

Cite this: DOI: 10.1039/d5nr03190g

Received 28th July 2025,
Accepted 4th August 2025

DOI: 10.1039/d5nr03190g

rsc.li/nanoscale

Quantitative biomechanical profiling of transformed human corneal epithelial cells†

Indrianita Lionadi, Liam McLarnon,‡ Gourav Bhattacharya, ‡ George A. Burke, Patrick Lemoine and Amir Farokh Payam *

Cell mechanics, governed by cortical surface dynamics and cytoskeletal viscoelasticity, evolve throughout the cell cycle, influencing cellular function and behavior. Using multimodal microscopy—bimodal atomic force microscopy (AFM), force mapping, and load-rate analysis—we investigate mechanical differences between mitotic and interphase human corneal epithelial-transformed cells (HCE-T). Our quantitative analysis reveals significant variations in stiffness, viscosity, adhesion, and loading-rate responses, reflecting the frequency- and time-dependent properties of cytoskeletal networks and intracellular fluid dynamics. We show that mitotic cells exhibit reduced stiffness in dynamic tests due to intracellular softening and increased fluidity, while static tests highlight cortical stiffening driven by contractile forces. These findings emphasize the dynamic interplay between actin and microtubules in regulating cellular mechanics during division. By integrating high-resolution mechanical mapping with advanced analytical techniques, this study provides novel insights into cytoskeletal remodeling, offering a robust platform for studying mechano-transduction with applications in regenerative medicine and tissue engineering.

Introduction

The human corneal epithelium plays a vital role in vision, contributing to two-thirds of the eye's focusing power and serving as a protective barrier to external insults.[1] Understanding its mechanical properties is essential for advancing ophthalmic research and addressing clinical challenges in corneal repair and regeneration. Corneal blindness affects approximately 4.2 million people globally,[2] yet only limited corneal transplants are performed,[3] highlighting the unmet need for engineered tissue solutions.[4] Advancing our understanding of corneal epithelial cellular mechanics offers a transformative potential for addressing these challenges and developing innovative therapies.[4]

While several studies have already been dedicated to understanding mechanics of the mitotic process[5–8] and macroscopic corneal biomechanics,[9–11] nanoscale and frequency-dependent mechanical properties of individual corneal epithelial cells remain largely unexplored, particularly during different stages of the cell cycle. Bridging this gap, we present a comparative study for quantifying the biomechanical properties of cells from the human corneal epithelial-transformed cell line (HCE-Ts), an established model system that replicates the morphological and biochemical characteristics of native corneal epithelial cells, with a focus on comparing mitotically dividing cells (mitotic cells) and resting cells (interphase cells). This model, derived from a 49-year-old patient,[12] exhibited hallmark features such as a cobblestone phenotype, desmosome formation, and expression of the 64 kDa cytokeratin, providing an ideal platform for studying nanoscale biomechanics.[13,14] Employing integrated multimodal atomic force microscopy (AFM),[15–17] we quantitatively analyzed the mechanical properties of HCE-T cells during mitosis and interphase. Utilizing bimodal AFM mapping, force spectroscopy, load-rate analysis and phase-contrast microscopy, we obtained a comprehensive biomechanical profile, including Young's modulus, adhesion, viscosity, loss tangent, dissipation, and 3D subsurface stiffness maps.

These measurements captured localized nanoscale variations in stiffness and viscoelasticity with unprecedented surface and subsurface sensitivity, revealing distinct mechanical differences across the cell cycle and the interplay between plasma membrane, cortical, and bulk cellular mechanics. Phase-contrast imaging identified mitotic and interphase cells, ensuring robust data collection at 80%–90% confluency. Complementary Raman spectroscopy validated chemical-mechanical correlations, reinforcing our observations. Fig. 1 illustrates our methodology, demonstrating the capability of

Nanotechnology and Integrated Bioengineering Centre, School of Engineering, Ulster University, BT15 1AP Belfast, UK. E-mail: a.farokh-payam@ulster.ac.uk

†This work is dedicated to the memory of Dr George A. Burke, whose scientific insight, mentorship, and collaboration greatly enriched this research. He will be deeply missed.

‡These authors have equal contributions.

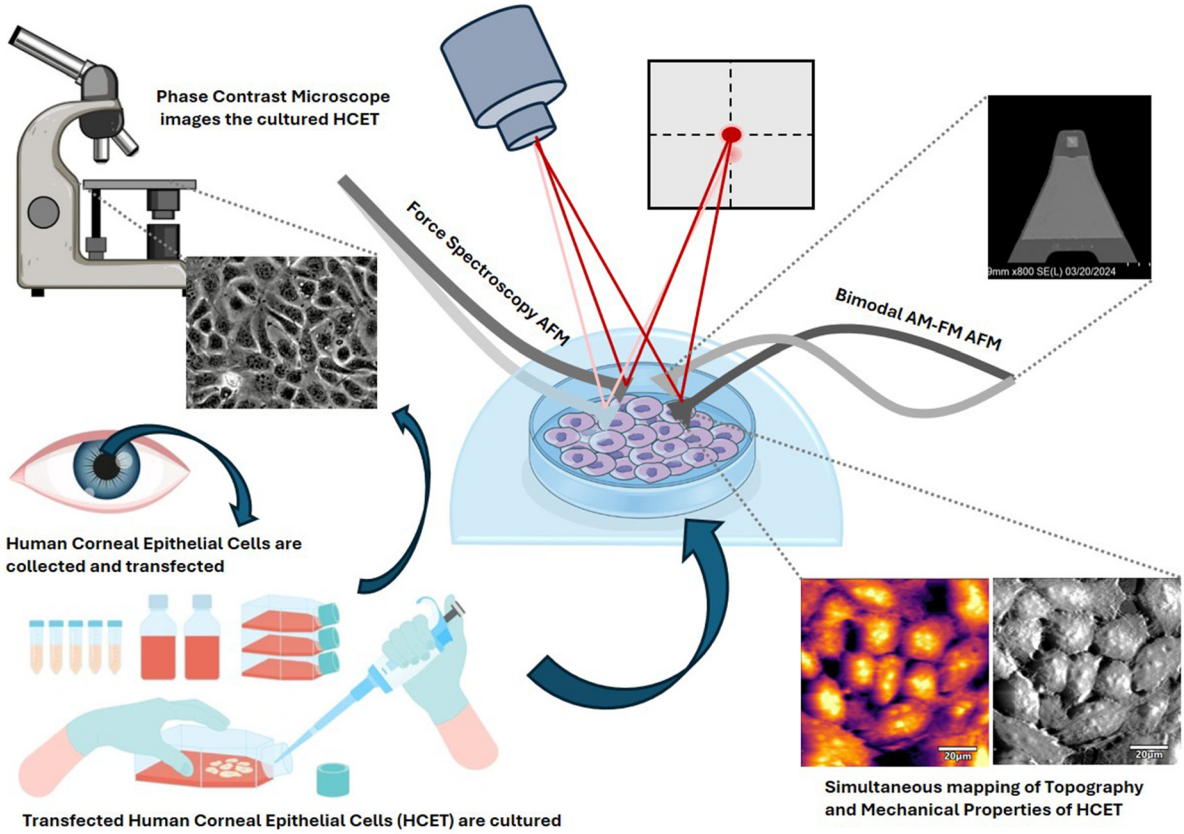

Fig. 1 Workflow scheme of the integrated microscopy methodology. The collected HCE-T cells are cultured under controlled conditions and utilized for both phase contrast imaging and integrated multimodal force microscopy characterization. The phase contrast microscope is employed to systematically monitor the confluency and morphological changes of the HCE-T cells over time. Simultaneously, the integrated force spectroscopy and bimodal AFM provide high-resolution data on the variations in cellular topography, structure, and nanomechanical properties. Additionally, this approach enables the generation of detailed 3D subsurface stiffness maps, capturing the dynamic mechanical transformations of the cells during their progression and differentiation. (Microscope by pikepicture, Human eye by Viktoriia Ablohina, Petri dish by Art of Science, Cell culture equipment by Pepermpron, all *via* Shutterstock).

our approach to accurately characterize cellular mechanics. To analyze the complex datasets, we integrated unsupervised learning algorithms and image correlation techniques, enabling pattern recognition and providing deeper insights into the mechanical behavior of corneal epithelial cells. By comparing quasi-static, dynamic, and time-dependent responses, our findings bridge a crucial gap in corneal research at specific scales and biomechanics at a larger scale, offering critical insights into epithelial cell mechanics that are foundational for tissue engineering and regenerative medicine.

Cell confluency and preparation for AFM measurements

During the initial phase of cell seeding, HCE-T confluency was monitored *via* phase contrast microscopy. Optimal confluency (70%–80% surface coverage) was reached after 72 hours, as shown in Fig. 2a–d and the SI Video. The time-lapse video shows that the rounded cells are growing and are not apoptotic or dead. Following this period, the cells were immediately subjected to a fixation protocol detailed in the methods section. Fixation is critical as it preserves the cellular morphology and structure, allowing for accurate and reproducible measurements during subsequent AFM assessments. While fixation increases the absolute stiffness due to protein cross-linking, this effect is consistent across all samples used in this study, allowing for valid comparative analysis between cell states. Moreover, fixation minimizes biological variability and enhances imaging stability—critical for high-resolution AFM measurements aimed at detecting intrinsic structural differences across the cell cycle.[18] Moreover, dynamic measurements on live cells often exhibit greater noise and drift, making it challenging to extract intrinsic material properties.[19]

At the post-fixation stage, the cells were prepared for AFM measurement, with the built-in optical microscope of the AFM system employed to further assess the cells on the glass substrate. This step, depicted in Fig. 2e, facilitated the precise selection of individual cells for targeted mechanical property measurements, ensuring that the samples chosen for analysis represented consistent experimental conditions. Fig. 2f shows the completed cell life cycle with real-time cell images, demonstrating the differentiable characteristics of the mitosis or mitotically active cells and the resting or interphase cells to be measured.

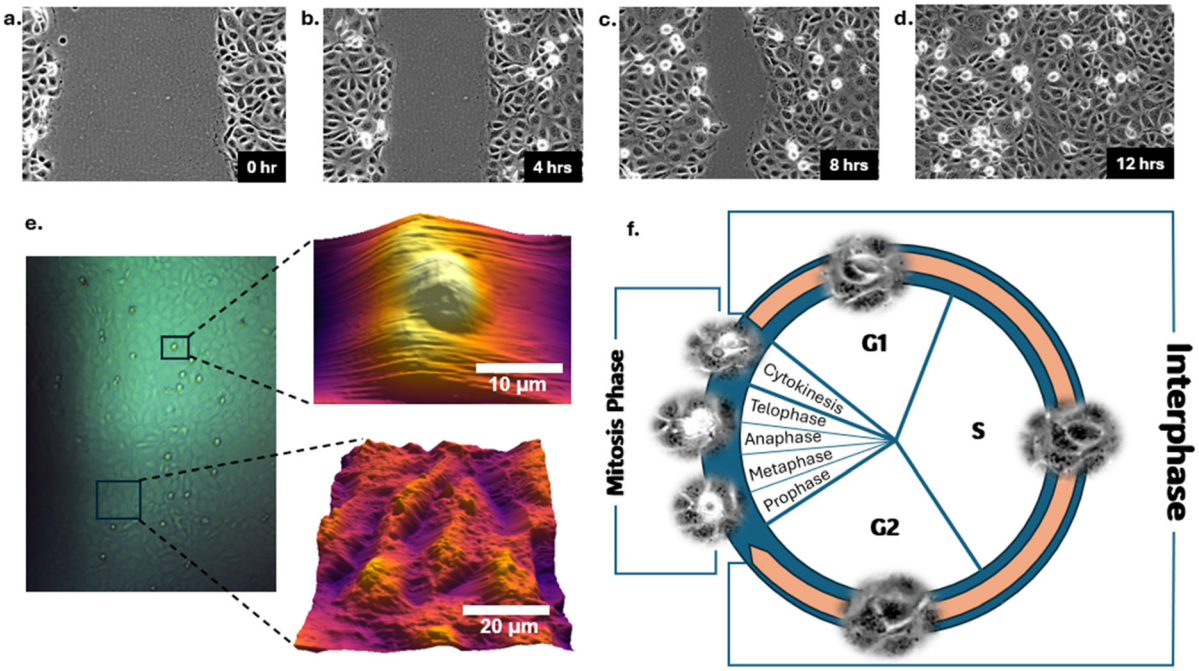

Fig. 2 Progression of HCE-T cell growth and differentiation monitored using phase contrast and optical imaging techniques. (a–d) Phase contrast images capturing the progressive growth of HCE-T cells from the initial seeding (0 hours) up to 12 hours, illustrating changes in cell morphology and adhesion over time. (e) Optical image of confluent HCE-T cells cultured on a glass substrate, taken using the built-in camera of the AFM system. This image serves as a reference for distinguishing between mitotic and interphase cells selected for measurement. (f) Schematic of the complete cell life cycle, complemented by real-time images of cells at different stages, offering insights into their dynamic transitions.

Mechanical property assessment using multifrequency AFM

Bimodal atomic force microscopy (AM–FM-AFM)[15] is a high-frequency technique that probes the mechanical properties of the plasma membrane, cortex, and cytoskeleton, offering insights into subsurface mechanics in soft matter.[16] It is highly sensitive to viscoelastic properties, capturing both elastic and viscous components, as well as dissipation at specific indentation depth.[20] This enables a comprehensive characterization of cell stiffness, particularly its dynamic mechanical behaviour. Additionally, simultaneous mapping of topography, Young's modulus, and indentation allows for subsurface stiffness mapping, providing localized, frequency-dependent mechanical insights.

We measured various locations across mitotic and interphase cells to ensure diversity in the mechanical properties, with representative results shown in the SI, S1 (Fig. S1–S3), and statistical histograms in Fig. 3a.ii–f.ii and g.ii–l.ii, as well as statistical average values listed in Table S1. The details of our statistical analysis are given in the Methods section.

As shown in Fig. 3a.i–f.i and g.i–l.i, we assessed mitotically dividing HCE-T and interphase cells using key biomechanical parameters, including Young's modulus, viscosity, loss tangent, and energy dissipation (quantification details are given in the Methods section). To account for the influence of the stiff glass substrate, which can constrain and limit cell deformation, we considered the bottom effect model in our quantification,[21,22] as explained in the Methods section and the SI, S2 (Fig. S4 and S5). To confirm cell deformability, we performed repeated measurements on the same cell, with a 4-minute interval, ensuring consistent mechanical properties over time (see the SI S3, Fig. S6). While consistent results from repeated measurements are expected in fixed samples, this nonetheless demonstrates the high accuracy of our quantification of cellular properties.

For mitotic cells under high-frequency measurements (25.8 to 26.8 kHz), Young's modulus ranged from 0.02 to 18.9 kPa, with the majority under 7 kPa (statistical average 5.49 ± 0.01 kPa). Mapping of the mechanical properties revealed scattered regions of softer and harder areas without a clear spatial pattern, possibly due to differences in cytoskeletal organization and cell adherence during mitosis.[23,24] Mechanical heterogeneity likely results from dynamic actin cytoskeleton remodeling, which regulates cell division, adhesion, and polarity. During mitosis, actin reorganizes to support chromosome segregation and cytokinesis, ensuring proper cell division and genomic stability. Disruptions in actin dynamics can lead to localized stiffness variations by affecting cell shape, adhesion, and force distribution.[23,24] The viscosity of cells in the mitosis phase ranged from 0.3 to 319 mPa s, with most below 100 mPa s (statistical average 0.08 ± 0.05 Pa s), highlighting the mechanical diversity linked to the cell cycle stage.[7] The loss tangent ranged from 0.39 to 3.35, with higher counts around 2 and an average of 1.69 ± 0.37 for all measured cells, indicating heterogeneous mechanical behavior during mitosis. The dissipation in the cells at mitosis phase displayed two distinct regions,

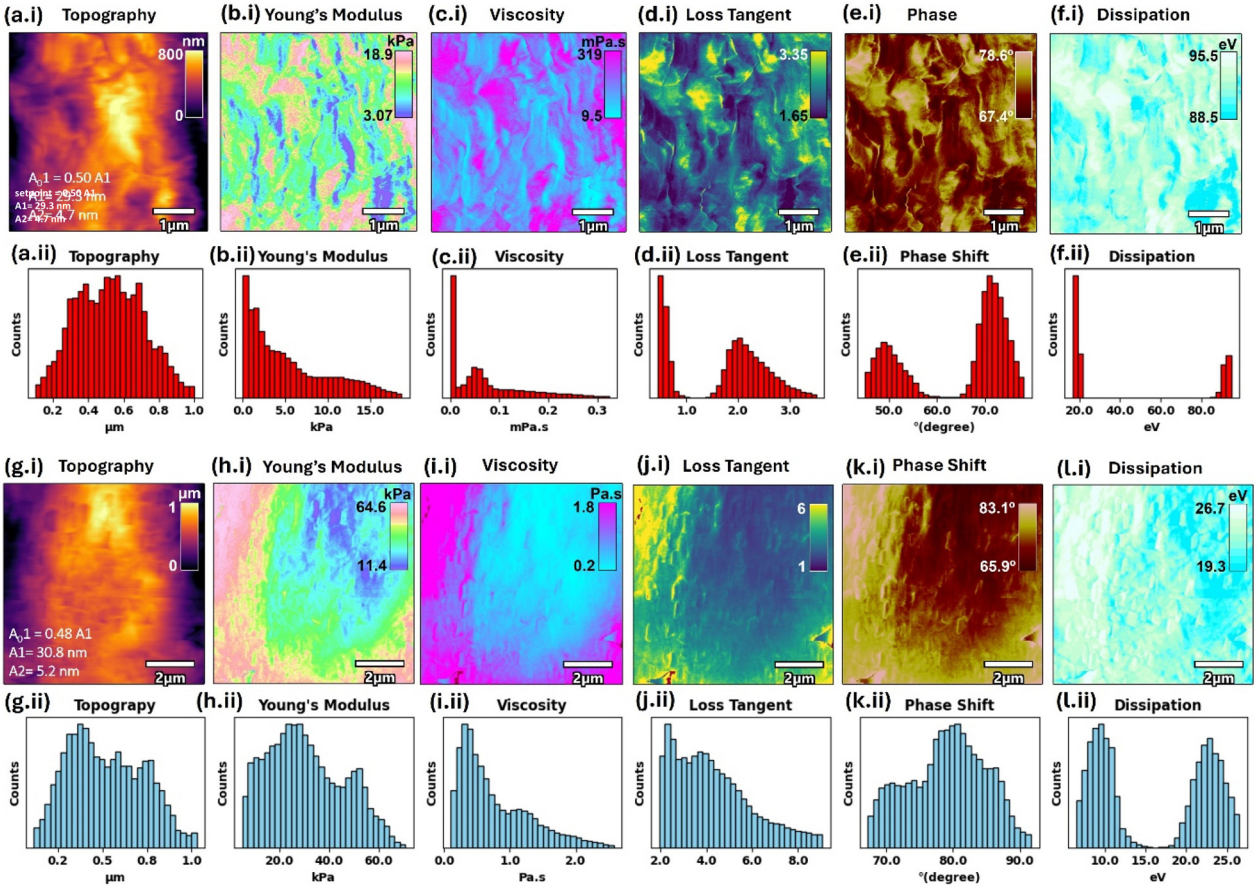

Fig. 3 Mechanical properties of mitotically dividing cells and interphase cells obtained from AM–FM bimodal measurements. (a.i–f.i) Topography, elasticity, viscosity, loss tangent, phase shift, and dissipation mapping of a mitotic cell, and the corresponding statistical histograms of the collective measurements done on mitotic cells (a.ii–f.ii). Identical reports depicted for interphase cells (g.i–l.i) for topography, elasticity, viscosity, loss tangent, phase shift and dissipation, and their corresponding statistical histograms (g.ii–l.ii). AM–FM measurement parameters are as follows: $A_{01} \sim 30$ nm, $A_2 \sim 5$ nm, $A_1 \sim 0.5A_{01}$, $f_1 \sim 26$ kHz, $f_2 \sim 66$ kHz. Note that for all histograms, the bin size was adjusted manually and determined to ensure visual clarity of the histograms.

one around 20 eV and the other around 90 eV, with a statistical average for all measured cells of 43 ± 1.05 eV, suggesting spatial variation in mechanical characteristics across the cortex and intracellular regions of cells under division, with active areas such as spindle poles[25] showing higher energy dissipation, and less active areas reflecting more stable properties. This points to the dynamic nature of cells in the mitosis phase with regionally varied mechanical properties.[24,26]

For cells at the interphase stage, Young's modulus ranged from 0.13 to 64.6 kPa, with a dominant range around 20 to 40 kPa (statistical average for all measured cells is 31.2 ± 0.04 kPa), showing a clear pattern of softer regions around the cell's center, consistent with the topography images. This softer region correlates with higher cell surface elevation, as cells at interphase states are mature, adherent, and spread across the substrate. Viscosity and loss tangent mappings of the resting cells corroborated the findings for Young's modulus. Higher viscosity values were associated with increased Young's modulus. For instance, the viscosities of cells at interphase state ranged from 0.06 to 1.82 Pa s (Fig. 3i. ii) with an average of 0.74 ± 0.5 Pa s for all measured cells, while the loss tangent ranged from 1 to 8.8 (Fig. 3j.ii) with an average of 4.5 ± 1.4 for all measured cells. This relationship between stiffness, viscosity, and loss tangent further supports the distinct mechanical behavior of the cells at interphase and mitosis phases and is in agreement with higher apparent viscosity values of interphase than mitotic cells reported for HeLa cells.[7] Interestingly, the energy dissipation of interphase cells is smaller than that seen in mitotic cells, as demonstrated in Fig. 3f.ii and l.ii. This difference reflects the more fluid-like behavior of mitotic cells, where the cell interior softens, and the dissipation increases.[6]

To understand the mechanical differences between mitotic and interphase HCE-T cells, we performed 3D subsurface mapping of Young's modulus and energy dissipation at varying indentation depths (Fig. 4). Under identical bimodal AFM conditions, mitotic cells exhibited greater indentation depths and lower Young's modulus than interphase cells, while their energy dissipation was higher at the corresponding

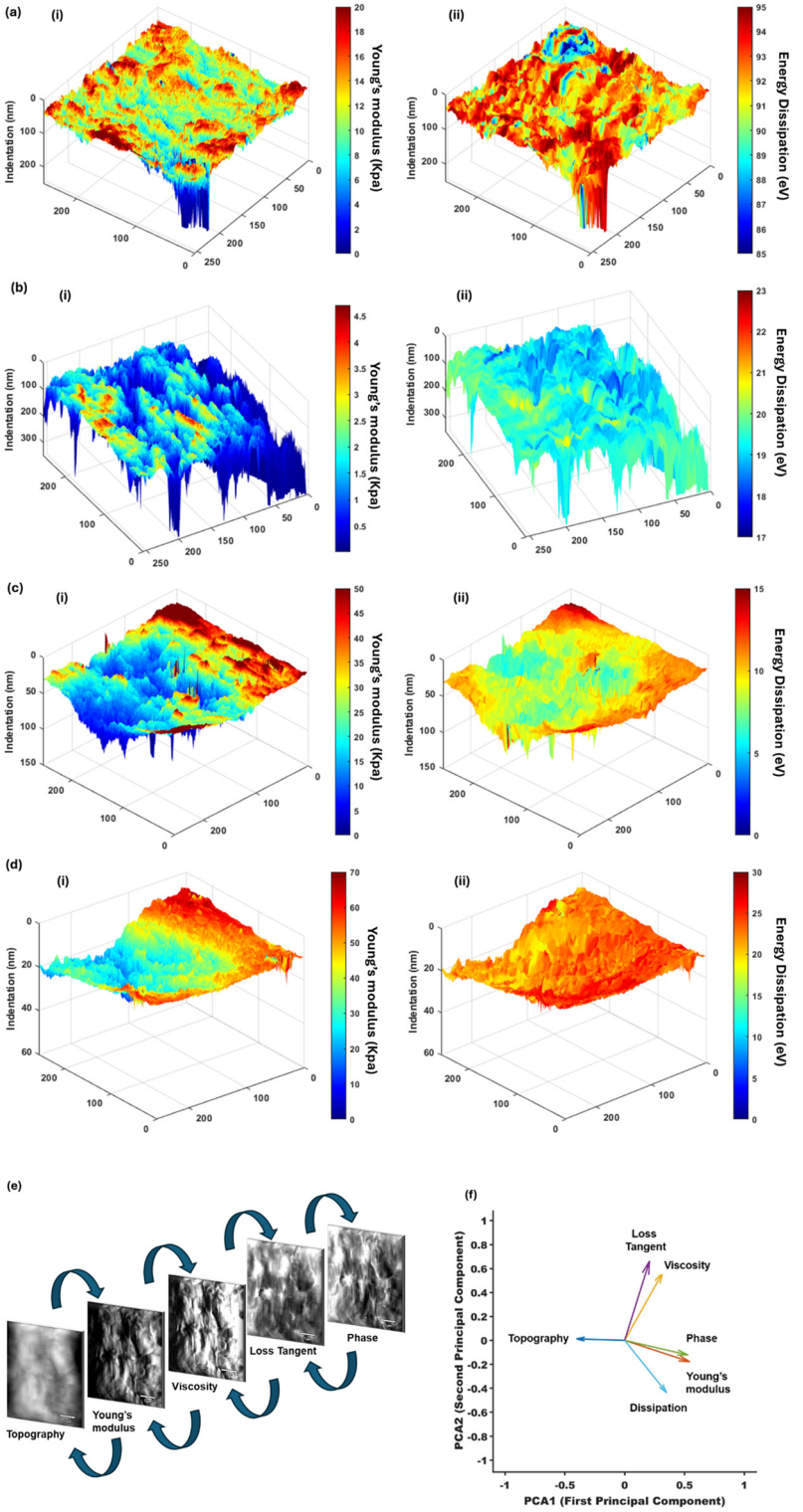

Fig. 4 Three-dimensional subsurface maps of (i) Young's modulus and (ii) energy dissipation of representative mitotic (a and b) and interphase (c and d) cells. The color bars represent values for Young's modulus (in kPa) and energy dissipation (in eV), while the *z* axis represents the indentation depth in (nm). The *x* and *y* axes present the 256 × 256 scanning pixels of the cell surface. (e) Workflow outlining the cross-correlation, PCA, and MVA data analysis applied to the measured data obtained from bimodal-AM–FM AFM. The analysis integrates advanced statistical and computational techniques to extract meaningful insights from the experimental data. (f) PCA results, illustrating the dimensionality reduction and the clustering patterns among the measured parameters.

depths. These findings highlight the distinct viscoelastic properties across the cell cycle. The increased deformability of mitotic cells results from cytoskeletal reorganization and intracellular softening.[6,23] Actin depolymerization and mitotic spindle formation reduce mechanical resistance, while cell rounding decreases substrate adhesion, further lowering the effective stiffness.[23] These factors explain the deeper indentation and lower Young's modulus of mitotic cells. In contrast, interphase cells maintain a dense, organized cytoskeleton with intact actin and intermediate filaments such as keratin,[27,28] which enhances stiffness and adhesion, leading to smaller indentation depths and higher Young's modulus. Their spread-out morphology and stronger adhesion to the substrate further enhance their resistance to deformation. These results are in contrast to previously reported stiffer values of mitotic cells under static measurements[7,8] and our quasi-static force mapping results, which will be discussed in the next section. Higher energy dissipation in mitotic cells aligns with their increased deformability and viscoelastic behavior.[6] Cytoskeletal remodeling and transient cytoplasmic flows contribute to higher dissipation at mitosis.[6,29] In interphase cells, the more stable cytoskeletal structure results in lower energy dissipation under similar conditions.

Comparing two mitotic cells reveals that at lower indentation depths (Fig. 4a and b), both Young's modulus and energy dissipation are higher due to cortical stiffening and strain-dependent mechanics.[5,6] As indentation increases, the cytoskeleton undergoes strain softening,[30] reducing stiffness and dissipation. A similar trend is observed in interphase cells (Fig. 4c and d), where lower indentations yield higher stiffness and dissipation, but greater indentations lead to cytoskeletal stretching and reduced mechanical resistance.[31] The observation of reduced Young's modulus with increasing indentation has been previously reported in AFM studies.[32] Bimodal AFM enhances sensitivity to these variations through high-frequency oscillations, which effectively probe viscoelastic properties. In mitotic cells, the dynamic reorganization of the cytoskeleton introduces lower stiffness and higher energy dissipation at high frequencies,[6] whereas interphase cells, with their more stable cytoskeletal structure, exhibit relatively low dissipation. All measurements were conducted under identical conditions in a liquid environment to ensure reproducibility. Phase mapping confirmed that the operation was within the repulsive regime, ensuring reliable quantification.

To analyze relationships among cellular properties from multifrequency measurements, we applied advanced data analysis techniques, including cross-correlation,[33] principal component analysis (PCA) and multivariate analysis (MVA)[34] (Fig. 4e and Fig. S7, with details in the SI, S4 and Methods sections).

PCA identified key patterns among six measured variables: topography, Young's modulus, viscosity, loss tangent, phase, and dissipation. PC1, derived *via* Horn's parallel analysis, captures shared variance in Young's modulus, phase, and dissipation, consistent with phase imaging theory in liquid AFM.[35] PC2, associated with loss tangent and viscosity, reflects distinct viscoelastic behaviors (Fig. 4f). The inverse relationship between topography and other parameters along PC1 reinforces its unique role in cellular mechanics. The PCA results align with the cross-correlation findings (Fig. S7a), clustering dissipation, phase, and Young's modulus as mechanical indicators that describe the interplay between elastic and dissipative interactions.[35] Similar trends were observed in separate PCA analyses for mitotic and interphase cells (see the SI, S4, Fig. S7c–f).

Furthermore, we performed statistical analysis to determine whether the Young's modulus values for cells in interphase and mitosis states come from the same population (see the SI, S5).

Force spectroscopy (mapping) measurements

Force mapping directly measures the force-displacement relationship at multiple points using a quasi-static cantilever in contact with the cell. In force spectroscopy, stiffness is derived from a contact mechanics model, where the applied force is measured as the cantilever deflects. The obtained values correspond to the cell's elastic modulus across indentation depths, influenced by local surface morphology.

Force spectroscopy was performed in a load control approach on mitotic and interphase cells using a Hertzian–Sneddon model[36] with a 500 nm AFM tip radius flat punch (see the SI, S6, Fig. S8). Young's modulus values obtained from the force mapping measurements ranged from 0.01 to 175 kPa (average: 34.96 ± 1.77 kPa) for mitotic cells and 0.3 to 70 kPa (average: 3.31 ± 1.68 kPa) for interphase cells, consistent with previous studies[25,29,31] (Fig. 5, Fig. S9 and Table S2). However, bimodal AFM measurements yielded different results, with mitotic cells averaging 5.49 ± 0.01 kPa and interphase cells 31.2 ± 0.04 kPa (Fig. 5e and j; Fig. S10). It is worth mentioning that, generally, our quantified Young's modulus is in the range of previously reported values for single corneal epithelial cells determined through load–displacement and friction-load measurements.[37,38]

Force mapping also revealed higher adhesion forces in mitotic cells (95.6 ± 4.5 pN) compared to interphase cells (50.5 ± 2.69 pN), reflecting increased membrane tension and adhesion molecule expression.[39] Stiffness and adhesion results, along with indentation ranges (Fig. S10), indicate that force mapping captures both bulk stiffness (cytoplasm mechanics) and surface stiffness (cell cortex and plasma membrane), aligning with reports of cortical stiffening during mitosis.[5,6]

The discrepancy between bimodal AFM and force mapping arises from their differing operational modes. Bimodal AFM, operating at high frequencies, is highly sensitive to nanoscale, localized viscoelastic properties, particularly subsurface fluid-like behavior.[6] In contrast, in our force mapping approach, we probe the entire indentation depth in static mode (Fig. S10), capturing integrated mechanical properties, including denser, organized actin networks in the mitotic cortex.[5,40] The apparent contradiction reflects their complementary nature: bimodal AFM highlights dynamic viscoelasticity, while force

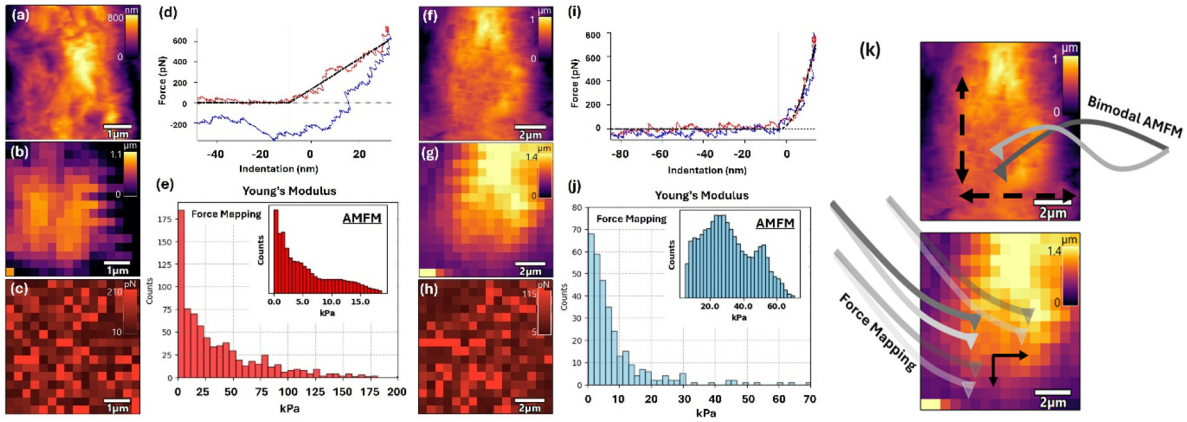

Fig. 5 (a) and (f) Topography of mitotic and interphase cells, respectively, obtained from AM–FM measurements. Force mapping was performed on the exact cell measured by bimodal AM–FM, giving the 16 × 16 pixels of topography and adhesion forces simultaneously generated from the force curve of each pixel; (b) and (c) for the mitotic cell depicted in (a) and (g) and (h) for the interphase cell shown in (f). Fitting of the force curve with the Hertzian flat punch contact mechanics model gives the Young's modulus values of each pixel, as shown in (d) and (i), as the representation of the force curve from the mitosis and interphase cell, respectively. The accumulative Young's modulus values gathered from several measurements are plotted in (e) for mitotic cells and (j) for interphase cells. The given inset on each plot shows the Young's modulus obtained from AM–FM methods. The visualization of the different work principle mechanisms between bimodal AM–FM and force mapping is depicted in (k).

mapping emphasizes quasi-static mechanical responses, providing distinct yet valuable insights into cellular mechanics.

Load rate analysis

The viscoelastic properties of biological cells are crucial for their deformation behavior and response to mechanical forces. To investigate these properties, we conducted a load-rate analysis using contact force spectroscopy on resting and mitotically dividing HCE-T cells. This analysis examined loading and pull-off forces (Fig. 6a.i). The loading force, derived from the approach curve, represents the force exerted on the AFM tip upon contact with the cell, indicating resistance to deformation (Fig. 6a.ii). The pull-off force, from the retraction curve, measures the force required to detach the AFM tip, reflecting adhesion forces (Fig. 6a.iii).

Under static conditions, mitotic cells exhibited higher loading forces than interphase cells, consistent with force mapping results indicating a denser actin cortex in dividing cells and cortex stiffening.[5,41] Interestingly, at higher loading rates, interphase cells showed greater forces, indicating a more dynamic mechanical response, in line with bimodal AFM results. These findings highlight the time-dependent mechanical behavior of cells and differences between mitotic and interphase states in both static and dynamic regimes.

We identified two loading-rate regimes. At low loading rates (<100 nN s^{-1}), the loading force decreased linearly with increasing loading rate, while the pull-off force increased, suggesting fluid-like, time-dependent deformation. At high loading rates (>100 nN s^{-1}), the cell response became nonlinear, with cells lacking time to adjust to the applied forces. This rapid deformation disrupted the actin filaments, reducing the cell's mechano-sensing capabilities, as seen by the fluctuation of the measured loading force.[42,43] Mitotic cells, with their enhanced rigidity at the cortex, were able to more effectively maintain the rounded shape necessary for division,[5,41] which explains the minimum fluctuation compared to those of the interphase cells.

Adhesion force measurements further differentiated the mechanical behavior of mitotic and interphase cells. Although interphase cells exhibited higher pull-off forces across varying loading rates (Fig. 6a.iii), force mapping revealed greater adhesion forces in mitotically active cells (Fig. 5c and h). This apparent contradiction arises from fundamental differences in the mechanical context, timescale, and deformation history between the two measurement modes. In load-rate experiments, the adhesion force reflects the strength of membrane–cytoskeleton coupling and the cell's ability to resist rapid detachment. Interphase cells, with their robust cortical actin network and stronger membrane–cytoskeleton anchoring, resist fast retraction more effectively, resulting in higher pull-off forces. In contrast, mitotic cells undergo cortical remodeling and lose focal adhesions during division, weakening cytoskeletal anchoring and reducing resistance to rapid detachment, which leads to lower pull-off forces in load-rate measurements.[24,27] Conversely, in quasi-static force mapping, the prolonged tip–membrane contact allows for different adhesion mechanisms to dominate. Despite cortex stiffening, mitotic cells exhibit increased membrane tension and a rounder morphology with reduced substrate adhesion, which increases the contact area and enables stronger tip–membrane interactions, particularly through membrane wrapping and lipid-mediated adhesion.[39] In contrast, the flatter morphology and stronger substrate anchoring of interphase cells limit membrane deformation and wrapping around the tip, reducing measurable adhesion forces during mapping. Together, these results highlight the stage-dependent differences in membrane–cytoskeleton architecture and their distinct contri-

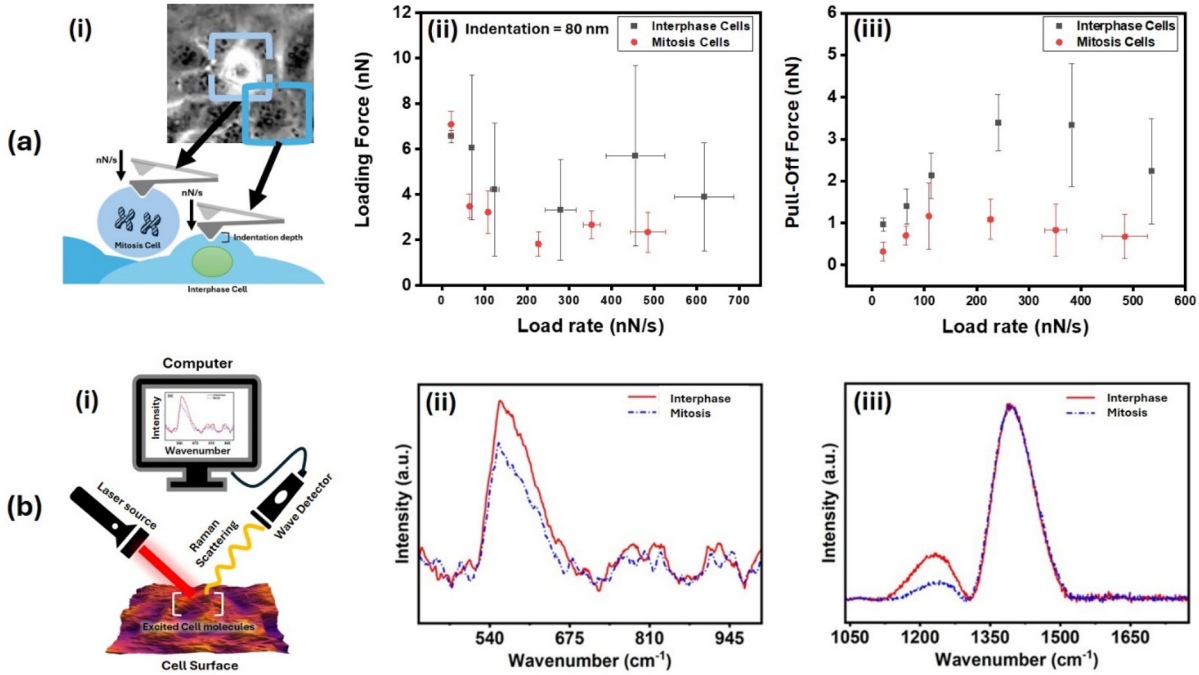

Fig. 6 (a) Graphs showing the relationship between load rate and loading force. (i) Schematic of the loading rate experiment on top of mitotic and interphase cells, and (ii) the load rate and (iii) the pull-off force of both resting and mitotically active cells. Bottom effect correction is applied to the loading force analysis and plotted in (ii) for the indentation depth of 80 nm for cells in both mitosis and interphase stages. (b) Schematic of the setup for the Raman spectroscopy measurement of cells (i) and the Raman spectra of interphase and mitosis cells scanned between (ii) 450–1000 cm^{-1} and (iii) 1000–1800 cm^{-1}.

butions to dynamic *versus* static adhesion regimes.[5,41] Fig. S11 shows a schematic of this cell cycle-dependent adhesion.

Raman spectroscopy analysis

Raman spectroscopy is a valuable tool for studying real-time changes in proteins, lipids, organelles, and nucleic acids, offering insights into the structural and functional transformations during the cell cycle.[44] To complement the mechanical assessments, Raman spectroscopy was performed on HCE-T cells to analyze biochemical changes during mitosis (Fig. 6b.i). Fig. 6b.ii and b.iii show the Raman spectra of interphase and mitotic cells, measured using a confocal system with sub-10-micron spatial resolution for single-cell analysis. The spectra display multiple peaks corresponding to various cellular components, consistent with existing literature.[45]

Key peaks include 490 cm^{-1} (glycogen)[46] which is known to be abundant in HCE-T cells,[47] 530–550 cm^{-1} (disulfide bonds in keratins and proteins[46]), 780 cm^{-1} (DNA ring-breathing mode[46]), 815 cm^{-1} (PO_2^- stretch of nucleic acids[48]), 940 cm^{-1} (C–C stretching in amino acids, specifically proline and valine[48]), 1205–1250 cm^{-1} (collagen and amide groups present in the collagens[49]), and 1367 cm^{-1} (bending mode of phospholipids[50]). The spectra were normalized, revealing major peaks with varying intensities between interphase and mitotic cells.

Keratin, a key structural protein in corneal epithelial cells,[28] is synthesized during interphase to maintain cytoskeletal integrity. During mitosis, protein synthesis is downregulated as cells prioritize the mechanics of division, including chromosome segregation and cytokinesis,[51] leading to reduced Raman peak intensity in mitotic cells. Similarly, collagen, abundant in the corneal epithelium,[52] maintains extracellular matrix (ECM) integrity in interphase[53] but experiences a temporary disruption during mitosis due to cellular reorganization.[54] Although collagen is not degraded, its stability is reduced during division, which is reflected in the decreased Raman intensity of the 1205–1250 cm^{-1} peak in mitotic cells. These findings align with the distinct mechanical properties observed in our AFM analysis.

Conclusion

This study investigates the mechanical properties of HCE-T cells during mitosis and interphase, revealing how their mechanical adaptation aligns with distinct functional stages of the cell cycle. Differences between static and dynamic measurements arise from the interplay between elastic and viscous components, which collectively shape the cellular responses to mechanical stimuli. Dynamic testing reveals that mitotic cells exhibit intracellular softening, fluid-like behavior, and increased energy dissipation, driven by actin cortex reorganization and cytoskeletal remodeling.[5,6,55] In contrast, static measurements indicate cortical stiffening, which reinforces the structural integrity and ensures proper chromosome segregation during division.[24,56,57]

During interphase, cells exhibit greater resistance to deformation due to an organized microtubule network, which stabilizes the cytoplasm and regulates intracellular mechanics.[58] In mitosis, however, mechanical properties are primarily governed by actin cortex dynamics rather than microtubule contributions, emphasizing the coordinated interplay between organelles, actin, and microtubules in force distribution.[6]

Reduced actin polymerization and myosin activity in mitotic cells contribute to cytoplasmic softening and decreased intracellular active energy, enabling fluid-like dynamics while maintaining cortical rigidity.[23,56] These adaptations ensure a balance between mechanical flexibility and structural stability, facilitating chromosome segregation while preserving cellular integrity.

Interestingly, these mechanical transformations resemble those observed during early embryogenesis, where actomyosin contractions and intracellular flows regulate morphogenetic processes.[6] Raman spectroscopy further supports our findings by demonstrating a consistent downregulation of keratin expression during mitosis, aligning with cytoskeletal remodeling and reduced stiffness.

Overall, this study highlights the complexity of cellular mechanics, emphasizing their dependence on measurement modalities, cytoskeletal architecture, and functional context within the cell cycle. These insights offer a deeper understanding of how cells regulate their mechanical state, with implications for mechanobiology, tissue engineering, and regenerative medicine.

Methods

Quantification of cell properties using bimodal AM–FM-AFM

In our bimodal AFM measurements, we have employed the bimodal amplitude modulation (AM)–frequency modulation (FM) technique called bimodal AM–FM.[15,20] From the bimodal AFM theory detailed in Amo *et al.*,[15] and Benaglia *et al.*,[20] considering the Hertz–Sneddon model for the tip–sample contact mechanics[36] and 3D Kelvin–Voigt model[20] for the contribution of viscoelastic force, the maximum indentation, the effective Young's modulus (storage modulus) and the viscosity (loss modulus) coefficient can be expressed as:

$$F = \frac{4}{3}E_{\text{eff}}\sqrt{R}\delta^{\frac{3}{2}} + 2\eta_{\text{com}}R\sqrt{\delta}\dot{\delta} \quad (1)$$

$$\delta_{\max} = (A_1k_1/2Q_1k_2)\cos\phi_1/(\Delta f_2/f_{02}) \quad (2)$$

$$E_{\text{eff}} = \left(4\sqrt{2}k_1Q_1/\sqrt{RA_1}\right)(k_2/k_1)^2(\Delta f_2/f_{02})^2/\cos^2\phi_1 \quad (3)$$

$$\eta_{\text{com}} = (2\pi\omega_1)^{-1}E_{\text{eff}}E_{\text{dis1}}/V_1 \quad (4)$$

where A_1 is the setpoints amplitude of the first mode, ω_1 is the angular resonance frequency of the first mode, f_{02} is the resonance frequency of the second mode, Δf_2 is the frequency shift of the second mode due to the interaction between the cantilever and cell, ϕ_1 is the phase shift of the first mode, R is the tip radius, Q_1 is the quality factor of the first mode, and k_1 and k_2 are the spring constants of the first and second modes, respectively. E_{dis1} and V_1 are the energy dissipation and virial of the first mode:[20]

$$E_{\text{diss1}} = \frac{\pi k_1A_1}{Q_1}(A_1 - A_{01}\sin\phi_1) \quad (5)$$

$$V_1 = \frac{k_1A_1A_{01}}{2Q_1}\cos\phi_1 \quad (6)$$

These expressions enable the bimodal AM–FM to generate images of the topography simultaneously with maps of the Young's modulus and viscosity coefficient. Also, it provides an opportunity to plot the subsurface map of stiffness *versus* maximum indentation at each scan point.

Furthermore, the loss tangent is obtained from:[20]

$$\tan\rho = \omega_1\frac{\eta_{\text{com}}}{E_{\text{eff}}} \quad (7)$$

Bottom effect correction

To consider the influence of the rigid substrate on the determination of the sample Young's modulus, the so-called bottom-effect artifact, we consider the following correction to the bottom-effect artifact yields the following force–indentation contact mechanics expression:[22]

$$F_{\text{GARCIA}} = F_{\text{SNEDDON}}\left[1 + \frac{1.133\sqrt{\delta R}}{h} + \frac{1.497\delta R}{h^2} + \frac{1.469\delta R\sqrt{\delta R}}{h^3} + \frac{0.755(\delta R)^2}{h^4}\right] \quad (8)$$

where h is the thickness of the cell deposited on the rigid substrate.

This leads to the correction in the Young's modulus equation and subsequently, the updated Young's modulus was used to calculate the viscosity and loss tangent from eqn (3) and (4):[21]

$$E_{\text{eff}} = \frac{\sqrt{8}}{\delta^2\sqrt{RA_1}}\frac{V_1}{1 + \frac{1.03\sqrt{\delta R}}{h} + \frac{1.25\delta R}{h^2} + \frac{1.14\delta R\sqrt{\delta R}}{h^3} + \frac{0.55(\delta R)^2}{h^4}} \quad (9)$$

Note that in the thickness measurements, we have used the following equation to consider the effect of the measured indentation in our thickness analysis:

$$h_{\text{true}}(x,y) = h_{\text{a}}(x,y) + \delta_{\max}(x,y) \quad (10)$$

where h_{a} is the thickness obtained from topography and $\delta_{\max}$ is the maximum indentation at each point.

Fig. S4 and S5 show the process of bottom-effect analysis and cell thickness measurements on our representative cell data.

HCE-T cell seeding

Human corneal epithelial cell culture. Human corneal epithelial cells (HCE-T) were sourced from the American Type Culture Collection (ATCC, USA) to ensure high-quality cell lines for our study. To initiate cell culture, a density of 2.5 ×

10^5 HCE-T cells was seeded onto a 2-well chamber slide (Nunc Lab-Tek II, USA). The cells were cultured in DMEM-F12 media supplemented with 5% fetal bovine serum (FBS) under controlled conditions of 37 °C and 5% CO_2 for 72 hours. This incubation period allowed the cells to adhere and proliferate adequately before proceeding to fixation, ensuring optimal cellular health for subsequent imaging and analysis.

HCE-T cell fixation. After the cell culture period, the HCE-T cells were carefully washed three times with phosphate-buffered saline (PBS) to remove any residual culture media. Fixation was achieved by treating the cells with 4% paraformaldehyde (PFA) for 20 minutes at room temperature. This fixation step was critical for preserving the intracellular structure and morphology. Following fixation, the PFA solution was removed, and the cells were washed three additional times with PBS to eliminate any unbound fixative. The fixed samples were subsequently stored at 4 °C in PBS until needed for atomic force microscopy imaging, ensuring that cellular integrity was maintained for precise mechanical characterization.

AFM measurement

Bimodal AMFM technique. To quantitatively assess the mechanical properties of the HCE-T cells, the bimodal amplitude-modulation frequency modulation technique was employed using a Jupiter XR atomic force microscope (Oxford Instruments, USA). This advanced AFM system facilitated the acquisition of experimental data and detailed quantitative imaging of the cells. The cantilever used in this study was an MLCT Bio-DC (D) (Bruker, USA), characterized by resonant frequencies ranging from 12–13 kHz f_1 and 78–80 kHz f_2 (in air) with corresponding spring constants of 0.033 N m^{-1} k_1 and 0.273 N m^{-1} k_2, determined using a thermal method. Under PBS, the resonant frequency is reduced to 3–4 kHz f_1 and 25–26 kHz f_2. Due to the poor quality factor of the f_1 in PBS, the bimodal AM–FM measurement was conducted using f_2 as f_1 and f_3 as f_2, given as ~26 kHz and ~66 kHz respectively. Quality factors measured in PBS solution were recorded as Q_1 = 2.1–6.7 and Q_2 = 6.9–12.2. The cantilever tip was previously flattened to a radius of 500 nm, enhancing the reproducibility of the mechanical quantification.

In addition to the AM–FM measurements, force spectroscopy mapping was conducted on the same cell surface to validate the obtained mechanical property data. Load rate analysis was performed by applying contact force spectroscopy with a range of tip velocities from 0.2 μm s^{-1} to 6 μm s^{-1}. These velocities were then converted into loading rates to analyse the deformation behaviour of the cells under varying mechanical stresses.

Raman spectroscopy. Raman spectra of both resting and mitotically dividing HCE-T cells were obtained using a Renishaw InVia™ Qontor® Raman Microscope. A 785 nm laser was employed for excitation, with an exposure time of 30 seconds and a laser power of 5 mW. This spectroscopic technique provided insights into the biochemical composition and structural properties of the cells, complementing the mechanical data gathered from the AFM measurements.

Statistical analysis. In our study, we analyzed 29 different cells in the interphase stage and 15 different cells in the mitosis stage. In our statistical analysis, we have considered two approaches.

In the first approach, our statistical strategy was designed to preserve the heterogeneity of cell mechanics across each population. Specifically, rather than extracting a single mean or median value per cell, we combined all the datapoints from all the measured cells within each group and provided the data range to construct comprehensive distributions of mechanical properties. This approach allows us to capture the full variability and complexity of cell surface mechanics, which would be partially masked by averaging at the single-cell level.

In the second approach, to provide a complete report, we extracted the mean values of individual mechanical maps from each cell and then calculated average values across the cell population. These final population-level averages are presented in Tables S1 and S2 in the SI.

Cross-correlation. Cellular features were analysed in terms of their cross-correlations for six key variables: topography, Young's modulus, viscosity, loss tangent, phase and dissipation. Two-dimensional cross-correlation (xcorr2) was used to quantify the spatial relationships between these features across all unique variable pairs. The resulting cross-correlation matrices provided insight into how the cellular features are interrelated, and these were visualized using a consistent colour scale for comparability. Peak cross-correlation values were identified to determine the strongest feature relationships, with the best resolution comparison reported based on the maximum observed cross-correlation.

PCA analysis. In this study, we also analysed a large number of cells to investigate their viscoelastic properties, focusing on the same 6 variables, to identify and visualize the key relationships among the cellular features. To ensure comparability across variables, the data were standardized using z-score normalization. Principal component analysis (PCA) was applied to identify the primary patterns of variation in these cellular features. The loadings of PCA1 and PCA2 for all 6 variables were then plotted against each other. The resulting visualization represents the average viscoelastic behaviour of the cells, illustrated through the loadings of the first two principal components.

MVA analysis. The interrelationships among the same six variables were investigated using a multivariate analytical approach. Data were sourced from text files, each containing matrices representing the variables. These matrices were transformed into vectors and compiled into a single data matrix, facilitating the calculation of pairwise Pearson correlation coefficients.

A correlation matrix was subsequently generated to quantify the linear associations among the variables, and a heatmap was created to provide a visual representation of these relationships. This methodology enabled a comprehensive assessment of variable interdependencies and served as a robust framework for multivariate analysis.

All computations were performed using MATLAB R2023b to ensure accuracy and reproducibility.

Conflicts of interest

There are no conflicts to declare.

Data availability

The data supporting the findings of this study are available in the main manuscript and its SI: raw bimodal AFM and force mapping results. See DOI: **https://doi.org/10.1039/d5nr03190g**.

If additional data are required, we are happy to provide them as SI.

Acknowledgements

This work was supported by the Department for the Economy (DfE), Northern Ireland, through the US-Ireland Research and Development Partnership under Grant USI 186.

References

1 M. A. Al-Aqaba, V. K. Dhillon, I. Mohammed, D. G. Said and H. S. Dua, Corneal nerves in health and disease, *Prog. Retinal Eye Res.*, 2019, **73**, 100762, DOI: **10.1016/j.preteyeres.2019.05.003**.
2 S. G. Gómez, *et al.*, Titanium Boston keratoprosthesis with corneal cell adhesive and bactericidal dual coating, *Biomater. Adv.*, 2023, **154**, 213654.
3 G. Xiao, B. C. Tsou, U. S. Soiberman, C. R. Prescott, D. Srikumaran and F. A. Woreta, Keratoplasty in the United States: Trends and Indications From 2015 to 2020, *Cornea*, 2023, **4**, 1360–1364.
4 K. Sadtler, *et al.*, Design, clinical translation and immunological response of biomaterials in regenerative medicine, *Nat. Rev. Mater.*, 2016, **1**, 16040.
5 M. P. Stewart, *et al.*, Hydrostatic pressure and the actomyosin cortex drive mitotic cell rounding, *Nature*, 2011, **469**, 226–231.
6 S. Hurst, B. E. Vos, M. Brandt and T. Betz, Intracellular softening and increased viscoelastic fluidity during division, *Nat. Phys.*, 2021, **17**, 1270–1276.
7 S. Abuhattum, *et al.*, An explicit model to extract viscoelastic properties of cells from AFM force-indentation curves, *iScience*, 2022, **25**(4), 104016.
8 A. V. Taubenberger, B. Baum and H. K. Matthews, The Mechanics of Mitotic Cell Rounding, *Front. Cell Dev. Biol.*, 2020, **8**, 687.
9 R. M. Gouveia, *et al.*, Assessment of corneal substrate biomechanics and its effect on epithelial stem cell maintenance and differentiation, *Nat. Commun.*, 2019, **10**, 496.
10 M. Wu, J. Han, X. Wang, T. Shao and Y. Wang, The alterations of corneal biomechanics in adult patients with corneal dystrophy, *Eye*, 2023, **37**, 492–500.
11 X. Wang, *et al.*, Assessment of corneal biomechanics, tonometry and pachymetry with the Corvis ST in myopia, *Sci. Rep.*, 2021, **11**, 3041.
12 K. Araki-Sasaki, *et al.*, An SV40-Immortalized Human Corneal Epithelial Cell Line and Its Characterization, *Invest. Ophthalmol. Visual Sci.*, 1995, **36**(3), 614–621.
13 A. Schermer, S. Galvin and T.-T. Sun, Differentiation-Related Expression of a Major 64K Corneal Keratin In Vivo and In Culture Suggests Limbal Location of Corneal Epithelial Stem Cells, *J. Cell Biol.*, 1986, **103**(1), 49–62.
14 E. Toropainen, in *Corneal Epithelial Cell Culture Model for Pharmaceutical Studies*, 2007.
15 C. A. Amo, A. P. Perrino, A. F. Payam and R. Garcia, Mapping Elastic Properties of Heterogeneous Materials in Liquid with Angstrom-Scale Resolution, *ACS Nano*, 2017, **11**, 8650–8659.
16 A. Farokh Payam and A. Passian, Imaging beyond the Surface Region: Probing Hidden Materials via Atomic Force Microscopy, *Sci. Adv.*, 2023, **9**, 26.
17 Y. F. Dufrêne, *et al.*, Imaging modes of atomic force microscopy for application in molecular and cell biology, *Nat. Nanotechnol.*, 2017, **12**, 295–307.
18 I. Sokolov, *et al.*, Noninvasive diagnostic imaging using machine-learning analysis of nanoresolution images of cell surfaces: Detection of bladder cancer, *Proc. Natl. Acad. Sci. U. S. A.*, 2018, **115**, 12920–12925.
19 C. R. Guerrero, P. D. Garcia and R. Garcia, Subsurface Imaging of Cell Organelles by Force Microscopy, *ACS Nano*, 2019, **13**, 9629–9637.
20 S. Benaglia, C. A. Amo and R. Garcia, Fast, quantitative and high resolution mapping of viscoelastic properties with bimodal AFM, *Nanoscale*, 2019, **11**, 15289–15297.
21 V. G. Gisbert and R. Garcia, Accurate Wide-Modulus-Range Nanomechanical Mapping of Ultrathin Interfaces with Bimodal Atomic Force Microscopy, *ACS Nano*, 2021, **15**, 20574–20581.
22 S. Chiodini, *et al.*, Bottom Effect in Atomic Force Microscopy Nanomechanics, *Small*, 2020, **16**, 2000269.
23 M. Dantas, J. T. Lima and J. G. Ferreira, Nucleus-Cytoskeleton Crosstalk During Mitotic Entry, *Front. Cell Dev. Biol.*, 2021, **9**, 649899.
24 P. Gibieža and V. Petrikaitė, The Regulation of Actin Dynamics during Cell Division and Malignancy, *Am. J. Cancer Res.*, 2021, **11**(9), 4050–4069.
25 J. Xie, J. Najafi, R. L. Borgne and M. Minc, Contribution of cytoplasm viscoelastic properties to mitotic spindle positioning, *Proc. Natl. Acad. Sci. U. S. A.*, 2021, **119**(8), e2115593119.
26 B. Sorce, *et al.*, Mitotic cells contract actomyosin cortex and generate pressure to round against or escape epithelial confinement, *Nat. Commun.*, 2015, **6**, 8872.
27 D. A. Fletcher and R. D. Mullins, Cell mechanics and the cytoskeleton, *Nature*, 2010, **463**, 485–492.
28 W. W. Y. Kao, Keratin expression by corneal and limbal stem cells during development, *Exp. Eye Res.*, 2020, **200**, 108206.

29 P. Bursac, *et al.*, Cytoskeletal remodelling and slow dynamics in the living cell, *Nat. Mater.*, 2005, **4**, 557–561.
30 A. M. Esfahani, *et al.*, Characterization of the strain-rate-dependent mechanical response of single cell-cell junctions, *Proc. Natl. Acad. Sci. U. S. A.*, 2021, **118**(7), e2019347118.
31 V. D. L. Putra, K. A. Kilian and M. L. Knothe Tate, Biomechanical, biophysical and biochemical modulators of cytoskeletal remodelling and emergent stem cell lineage commitment, *Commun. Biol.*, 2023, **6**, 75.
32 M. Lekka, Applicability of atomic force microscopy to determine cancer-related changes in cells, *Philos. Trans. R. Soc., A*, 2022, **380**(2232), DOI: **10.1098/rsta.2021.0346**.
33 A. Belianinov, S. V. Kalinin and S. Jesse, Complete information acquisition in dynamic force microscopy, *Nat. Commun.*, 2015, **6**, 6550.
34 A. F. Payam, B. Kim, D. Lee and N. Bhalla, Unraveling the liquid gliding on vibrating solid liquid interfaces with dynamic nanoslip enactment, *Nat. Commun.*, 2022, **13**, 6608.
35 A. F. Payam, J. R. Ramos and R. Garcia, Molecular and nanoscale compositional contrast of soft matter in liquid: Interplay between elastic and dissipative interactions, *ACS Nano*, 2012, **6**, 4663–4670.
36 A. N. Ahmine, M. Bdiri, S. Féréol and R. Fodil, A comprehensive study of AFM stiffness measurements on inclined surfaces: theoretical, numerical, and experimental evaluation using a Hertz approach, *Sci. Rep.*, 2024, **14**, 25869.
37 J. P. Straehla, *et al.*, Nanomechanical probes of single corneal epithelial cells: Shear stress and elastic modulus, *Tribol. Lett.*, 2010, **38**, 107–113.
38 S. Masterton and M. Ahearne, Mechanobiology of the corneal epithelium, *Exp. Eye Res.*, 2018, **177**, 122–129.
39 D. Raucher and M. P. Sheetz, Membrane Expansion Increases Endocytosis Rate during Mitosis, *J. Cell Biol.*, 1999, **144**, 497–506.
40 Y. W. Heng and C. G. Koh, Actin cytoskeleton dynamics and the cell division cycle, *Int. J. Biochem. Cell Biol.*, 2010, **42**, 1622–1633.
41 E. Fischer-Friedrich, *et al.*, Rheology of the Active Cell Cortex in Mitosis, *Biophys. J.*, 2016, **111**, 589–600.
42 X. Sun and G. M. Alushin, Cellular force-sensing through actin filaments, *FEBS J.*, 2023, **290**, 2576–2589.
43 K. Ohashi, S. Fujiwara and K. Mizuno, Roles of the cytoskeleton, cell adhesion and rho signalling in mechanosensing and mechanotransduction, *J. Biochem.*, 2017, **161**, 245–254.
44 K. V. Serebrennikova, A. N. Berlina, D. V. Sotnikov, B. B. Dzantiev and A. V. Zherdev, Raman scattering-based biosensing: New prospects and opportunities, *Biosensors*, 2021, **11**(12), 512.
45 Z. Movasaghi, S. Rehman and I. U. Rehman, Raman spectroscopy of biological tissues, *Appl. Spectrosc. Rev.*, 2007, **42**, 493–541.
46 N. Stone, C. Kendall, J. Smith, P. Crow and H. Barr, Raman spectroscopy for identification of epithelial cancers, *Faraday Discuss.*, 2004, **126**, 141–157.
47 H. Peng, J. Katsnelson, W. Yang, M. A. Brown and R. M. Lavker, FIH-1/c-kit signaling: A novel contributor to corneal epithelial glycogen metabolism, *Invest. Ophthalmol. Visual Sci.*, 2013, **54**, 2781–2786.
48 W. T. Cheng, M. T. Liu, H. N. Liu and S. Y. Lin, Micro-Raman spectroscopy used to identify and grade human skin pilomatrixoma, *Microsc. Res. Tech.*, 2005, **68**, 75–79.
49 A. Rygula, *et al.*, Raman spectroscopy of proteins: A review, *J. Raman Spectrosc.*, 2013, **44**, 1061–1076.
50 R. Jyothi Lakshmi, V. B. Kartha, C. Murali Krishna, J. G. R. Solomon, G. Ullas and P. Uma Devi, Tissue Raman Spectroscopy for the Study of Radiation Damage: Brain Irradiation of Mice, *Radiat. Res.*, 2002, **157**, 175–182.
51 A. Lindqvist, V. Rodríguez-Bravo and R. H. Medema, The decision to enter mitosis: feedback and redundancy in the mitotic entry network, *J. Cell Biol.*, 2009, **185**, 193–202, DOI: **10.1083/jcb.200812045** (preprint).
52 M. M. Islam, *et al.*, An in vitro 3-dimensional Collagen-based Corneal Construct with Innervation Using Human Corneal Cell Lines, *Ophthalmol. Sci.*, 2024, **4**(6), 100544.
53 K. E. Kadler, D. F. Holmes, J. A. Trotter and J. A. Chapman, Collagen Fibril Formation, *Biochem. J.*, 1996, **316**, 1–11.
54 I. Becher, *et al.*, Pervasive Protein Thermal Stability Variation during the Cell Cycle, *Cell*, 2018, **173**, 1495–1507.
55 R. Sakamoto and M. P. Murrell, Mechanical power is maximized during contractile ring-like formation in a biomimetic dividing cell model, *Nat. Commun.*, 2024, **15**, 9731.
56 M. G. Andrews, L. Subramanian, J. Salma and A. R. Kriegstein, How mechanisms of stem cell polarity shape the human cerebral cortex, *Nat. Rev. Neurosci.*, 2022, **23**, 711–724.
57 E. Fischer-Friedrich, *et al.*, Rheology of the Active Cell Cortex in Mitosis, *Biophys. J.*, 2016, **111**, 589–600.
58 Z. Kechagia and P. Roca-Cusachs, Cytoskeletal safeguards: Protecting the nucleus from mechanical perturbations, *Curr. Opin. Biomed. Eng.*, 2023, **28**, 100494.